ORIGINAL RESEARCH ARTICLE

INDUCTANCE CALCULATION OF CONCENTRATED AND DISTRIBUTED WINDING SYNCHRONOUS RELUCTANCE MOTOR USING MODIFIED WINDING FUNCTION THEORY

A. M. Epemu and B. E. Nyong-Bassey

Department of Electrical and Electronic Engineering, Federal University of Petroleum Resources Effurun, Nigeria.
Corresponding author's email address: epemu.ayebatonye@fupre.edu.ng

ARTICLE INFORMATION	ABSTRACT
	This study evaluates the inductance characteristics of synchronous reluctance motors (SynRMs) with concentrated and distributed windings. Two methods based on Winding Function Theory (WFT) are used: the sinusoidal method and the actual winding function method. The actual winding function method, which considers spatial harmonics and actual geometry, is found to be more accurate. The study reveals that the distributed winding SynRM has a higher saliency ratio (2.10) compared to the concentrated winding SynRM (1.58), indicating better performance. These findings contribute to our understanding of SynRM inductance and can guide improvements in motor design and performance. The study also suggests avenues for developing more precise inductance calculation methods for SynRMs, enabling optimized motor performance.

1.0   Introduction

Winding Function Theory (WFT) is a widely used method for calculating inductances in various types of machines, considering factors such as configurations, eccentricities, and airgap lengths as presented by Faiz and Tabatabaei (2002). It has been successfully applied in studies on synchronous and asynchronous machines, variable speed doubly-fed reluctance machines, and induction machines with spatial harmonics and rotor bar skewing as seen in Liang et al. (1991) and Gojko et al. (1999).

To address specific challenges, a modified version of WFT called Modified Winding Function Theory (MWFT) was proposed. MWFT enables the modelling of airgap eccentricity in synchronous machines, providing accurate results as presented by Al-Nuaim and Toliyat (1998).

Researchers have combined WFT with direct phase quantities to analyze synchronous generators under internal faults, effectively considering asymmetries and spatial harmonics in Jiang et al. (1999). Additionally, a global method based on WFT was developed for simulating faulty induction machines, including stator and rotor faults, as well as airgap eccentricities. This method can also be extended to synchronous machines as presented by Houdouin et al. (2003).

MWFT has been employed to model synchronous generators with dynamic eccentricity, yielding results consistent with finite element analysis (FEA) by Faiz and Tabatabaei, (2002) and Tabatabaei et al. (2004). Obe (2009) proposed a direct numerical procedure based on WFT to accurately calculate inductances in synchronous reluctance machines, incorporating actual geometry and

winding placements. This approach has also been applied to cage-less synchronous reluctance machines, considering stator windings and cross-coupling effects in Obe et al. (2009).

Furthermore, Obe (2010) extended the application of WFT to calculate torque and inductances in axially laminated synchronous reluctance machines, considering saturation effects, rotor lamination insulations, and stator slots. The full-order model based on WFT showed better agreement with FEA compared to the sinusoidal model.

The performance of synchronous reluctance machines is influenced by inductance values along the direct and quadrature axes, impacting torque capability and the saliency ratio (Spargo, 2016). The present study aims to calculate inductances for concentrated and distributed winding synchronous reluctance motor models using both the sinusoidal and actual winding function methods. The d-axis and q-axis inductances will be comparatively analyzed to determine the model with superior performance.

In summary, this study aims to contribute to the understanding of inductance characteristics in synchronous reluctance motors with concentrated and distributed windings. By utilizing WFT-based methods, the study provides a comprehensive numerical comparison of inductances, facilitating the design and optimization of motor performance.

2.0   Materials and Methods
2.1   Modified Winding Function Theory for machines with salient pole rotor

In conventional winding function theory, the air gap function is assumed to be composed of only even harmonics. Figure 1 presents a machine with two-pole winding residing within the air gap. The winding function theory was amended in this section to include machine geometries with salient poles, this will be termed the Modified winding function theory.
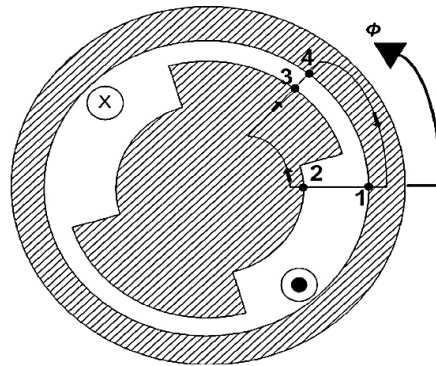
Figure 1: An ideal machine with a salient pole rotor.

According to Lipo (2012), by applying Ampere's law, the line integral is taken along the path of the conductor 1-2-3-4-1 as shown in equation (1), going along the path around the conductor in Figure 1, and the total MMF is calculated as seen in equation (2).

$$\oint H \cdot dl = \int J \cdot ds \qquad (1)$$

$$M_{12} + M_{23} + M_{34} + M_{41} = n(\phi)i \qquad (2)$$

The MMF drops are equivalent to the turns function $n(\phi)$ multiplied by the current, i in the winding. As with the case of the conventional winding function theory, linear iron is assumed to have high relative permeability; thus, MMF drops in the stator and rotor iron are negligible and ignored. The turns function will account for the changing MMF throughout the machine, as in the case of the cylindrical rotor, while the inverse air gap function will be used to account for the changing air gap thickness.

The magnetic field intensity $H(\phi)$ can be evaluated to form equation (3) if $M(\phi)$ can be assigned to be the MMF of the inner stator surface to the rotor pole, and the entire surface can now be taken to be at the same magnetic potential.

$$\int_0^{2\pi} M(\phi)g^{-1}(\phi)d\phi = 0 \tag{3}$$

From the assumptions in (3), the value of the MMF can be given as follows:

$$\int_0^{2\pi} \left[M_{12}(0) + M_{34}(\phi)\right] g^{-1}(\phi)d\phi = \int_0^{2\pi} n(\phi)g^{-1}i(\phi)d\phi \tag{4}$$

To find the right term in Equation (4), assuming the left term is equal to zero;

$$2\pi M_{12}(0)\left\langle g^{-1}(\phi)\right\rangle = \int_0^{2\pi} n(\phi)g^{-1}i(\phi)d\phi \tag{5}$$

$$M_{12}(0) = \frac{1}{2\pi\left\langle g^{-1}(\phi)\right\rangle} \int_0^{2\pi} n(\phi)g^{-1}i(\phi)d\phi \tag{6}$$

$$M_{12}(0) + M_{34} = n(\phi)i \tag{7}$$

$$M_{12}(0) + M_{34}(\phi) = n(\phi)i \tag{8}$$

$$M_{34}(\phi) = \left[n(\phi) - \frac{1}{2\pi\left\langle g^{-1}(\phi)\right\rangle} \int_0^{2\pi} n(\phi)g^{-1}i(\phi)d\phi\right] i \tag{9}$$

$$\left\langle M(\phi)\right\rangle = \frac{1}{2\pi\left\langle g^{-1}(\phi)\right\rangle} \int_0^{2\pi} n(\phi)g^{-1}i(\phi)d\phi \tag{10}$$

$$M(\phi) = n(\phi) - \left\langle M(\phi)\right\rangle \tag{11}$$

Note that equation (11) is known as the modified winding function, which shows that a new average value $\left\langle M(\phi)\right\rangle$ will be subtracted from the turns function $n(\phi)$.

If two windings A and B with radius *r* and stack length *l*, new inductance values can be gotten using the modified winding function theory as shown in equation (12), for self or magnetizing inductance and equation (13) for mutual inductance.

$$L_{AA} = \frac{\lambda_{AA}}{i_A} = \frac{\mu_0 rl}{g} \int_0^{2\pi} n_A(\phi) M_A(\phi) g^{-1} d\phi \qquad (12)$$

$$L_{AB} = \frac{\lambda_{AB}}{i_B} = \frac{\mu_0 rl}{g} \int_0^{2\pi} n_A(\phi) M_B(\phi) g^{-1} d\phi \qquad (13)$$

Note that the flux linkage λ_{AA} is the flux in winding A, due to its current, and the flux linkage λ_{AB} is due to the current in winding B, it should also be noted that these equations employ a product of winding functions and turns functions.

Since the inverse air gap function $\langle g^{-1}(\phi) \rangle$ contains even harmonics for conventional WFT and when the winding functions are expressed in odd harmonics, a new equivalent mutual inductance will be given as presented in equation (14)

$$L_{AB} = \frac{\mu_0 rl}{g} \int_0^{2\pi} M_A(\phi) M_B(\phi) g^{-1} d\phi \qquad (14)$$

While that of self or magnetizing inductance will be given as seen in equation (15)

$$L_{AA} = \frac{\mu_0 rl}{g} \int_0^{2\pi} M_A^2(\phi)(\phi) g^{-1} d\phi \qquad (15)$$

For synchronous reluctance machines, where the reference position for the angle ϕ, is chosen as the axis on phase A, θ_r is defined as the point of symmetry on one of the two-pole faces relative to the axis of phase A, the magnetizing inductance for phase A, is given in equation (16):

$$L_{AA} = \mu_0 rl \int_0^{2\pi} N_A^2(\phi) g^{-1}(\phi, \theta_r) d\phi \qquad (16)$$

The inverse air gap function dependency on the rotor position was explicitly shown in equation (16). Since $N_A^2(\phi)$ is a constant equal to $N_t^2/4$ where N_t is the total number of turns per pole per phase, equation (16) can now be written as presented in (17)

$$L_{AA} = \mu_0 rl \left(\frac{N_t^2}{4} \right) \int_0^{2\pi} g^{-1}(\phi, \theta_r) d\phi \qquad (17)$$

The formula for the calculation of mutual inductance for a synchronous reluctance machine is quite more complicated than that of self-inductance.

Corresponding author's e-mail address: epemu.ayebatonye@fupre.edu.ng

$$L_{AB} = \mu_0 rl \int_0^{2\pi} n_A(\phi) N_B(\phi) g^{-1}(\phi, \theta_r) d\phi \qquad (18)$$

As shown in equation (18), the product of the turns function in winding A and the winding function of winding B is used to multiply the inverse air gap function θ_r. Note the inverse air gap function is plotted for an arbitrary value $0 < \theta_r < \pi/2$.

2.2 Machine description

A three-phase synchronous reluctance machine with a traditional dumbbell salient pole rotor, having a p number of poles and three-phase windings *'abc'* will be modelled using analytical expressions representing the air gap and the windings. The number of poles p is the same as the number of poles on the rotor (Figure 2), with dimensions presented in Table 1.
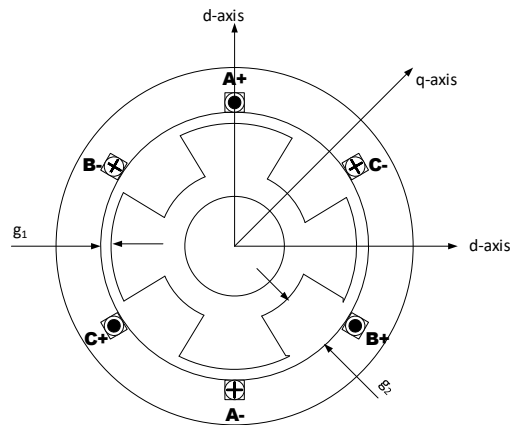
Figure 2: Three-phase four-pole Synchronous reluctance machine

Table 1. Machine dimensions of the SynRM extrapolated from Obe, (2009)

Machine dimensions	Values	
Stator outer radius	105.2mm	
Stator inner radius	67.99mm	
Rotor radius	67.69mm	
Effective stack length	160.22	
Airgap length at pole face, g_1	0.4mm	
Airgap length between poles, g_2	21.3mm	
Stator slot depth	18mm	
Ratio of pole arc to pole pitch	2/3	
Number of Pole pairs	2	
Winding connection	Y	
Number of winding layers	1	
	Distributed winding	Concentrated winding
Number of slots	36	12
Number of turns	32	96
Stator slot pitch	10°	30°

The study considered two machine models: (a) a proposed 12-slot full-pitch single-layer concentrated winding and (b) a proposed 36-slot full-pitch single-layer distributed winding, with dimensions shown in Table 1. Figure 3 depicts the winding clock diagrams. A traditional dumbbell rotor with damper windings was used.
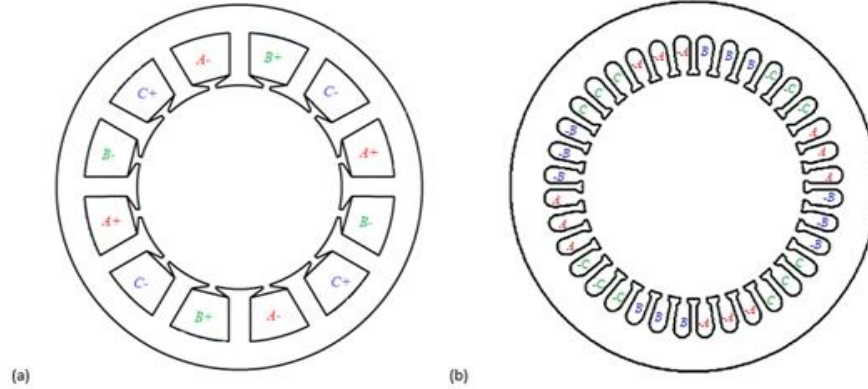
Figure 3: Winding clock diagrams of (a) concentrated winding SynRM (b) distributed winding SynRM

2.3 Stator Winding Function

The determination of machine inductances is crucial as it defines the behaviour of the SynRM since it influences the reluctance torque of the SynRM, using the expression for the calculation of stator self and mutual inductances presented in equations (17) and (18).

Using Fourier series, the winding expression of an arbitrary phase A, of an m-phase machine with P_p pole pairs can be written as

$$N_A(\phi) = \sum_{n=1,3,5,\dots}^{\infty} \frac{4 N_t k_{wn}}{P_p n \pi} \cos P_p n (\varphi - \kappa \frac{2\pi}{mP_p}) \tag{19}$$

Where, $k = 0, 1, 2$, for phases A, B, and C respectively, showing the phase shift of the various phases, N_t is the number of turns per pole per phase, P_p is the number of pole pairs, n is the harmonic order, m is the number of phases, φ is the stator circumferential position and k_{wn} is the winding factor for the nth harmonic as seen in Obe (2010).

According to Obe and Binder (2011), for the actual winding function model, the stator winding expression N_A of an arbitrary phase A, at the kth data point is shown in equation (20).

$$N_A(k) = n_A(k) - \frac{\sum_{k=1}^{n} n_A(k)}{n} \tag{20}$$

where, $n_A(k)$ is the turns function.

2.4 Airgap Winding Function

The airgap expression in equations (17) and (18) is dependent on the nature of the rotor geometry. As stated earlier, the rotor used in this machine is the traditional dumbbell rotor.

In the sinusoidal model, the air gap will be modelled using the Fourier series as presented in Equation (21)

$$g(\phi, \theta_r) = k_c g_1 + \beta k_c (g_2 - g_1) + \frac{2}{\pi} \sum_{n=1}^{\infty} \frac{1}{n} k_c (g_2 - g_1) \times \sin n\beta\pi \cos 2P_p n(\phi - \theta_r)$$

(21)

Where g_1 and g_2 are the airgap at the pole face and between poles, β is the pole arc to pole pitch ratio, k_c is the Carter coefficient, accounting for slot openings, θ_r is the angular position of the rotor and ϕ is the stator circumferential position.

The actual airgap of the synchronous reluctance machine having a traditional dumbbell rotor, with all harmonics included was modelled the same way as presented in Obe (2009).

2.5 Rotor Cage Winding Function

The stator-to-rotor mutual inductances were determined using equation (18), but the rotor cage winding expression in the rotor reference frame will be used.

The fundamental (sinusoidal d-q) components of the d-axis and q-axis rotor winding expression derived from Lipo (2012), are shown in equations (22) and (23)

$$N_{dr}(\varphi, \theta_r) = \frac{2}{\pi}\left[n_m + 2\sin^2\frac{\gamma}{2} - \frac{\sin(n_m\gamma)\cos(n_p\gamma)}{\sin\gamma}\right]\sin\xi$$

(22)

$$N_{qr}(\varphi, \theta_r) = \frac{8}{\pi}\left[n_m - \frac{\cos\left(\gamma\frac{n_b-1}{2}\right)\sin(n_m\gamma)}{\sin\gamma}\right]\sin^2\frac{\gamma}{2}\cos\xi$$

(23)

where $n_m = 1/2(n_b - 2)$, $n_p = 1/2(n_b + 2)$, n_b is the number of rotor bars per pole, γ is an angle known as the rotor slot span and $\xi = (\varphi - \theta_r)$.

The actual rotor winding expression is presented in equations (24) and (25) as seen in (Lipo, 2017)

$$N_{dr}(\phi) = \frac{4}{\pi}\sin^2\left(\frac{\gamma}{2}\right) + \frac{4}{\pi}\sin^2\left(\frac{3\gamma}{2}\right) + \frac{4}{\pi}\sin^2\left(\frac{5\gamma}{2}\right)$$

(24)

$$N_{qr}(\phi) = \frac{4}{\pi}\left[\cos\frac{\gamma}{2} - \cos\frac{3\gamma}{2}\right]^2 + \frac{4}{\pi}\left[\cos\frac{3\gamma}{2} - \cos\frac{5\gamma}{2}\right]^2$$

(25)

2.6 Inductance Calculation

The stator winding functions, the rotor cage winding functions and the airgap functions were used in calculating the stator self and mutual inductances, and also the stator to rotor mutual inductances as presented in equations (17) and (18).

The sinusoidal winding function model was used in the combination of sinusoidal winding expression as shown in equation (19), and the airgap function as corrected by Carter's factors

considering only the second harmonic as shown in equation (21). The actual winding function model used winding expressions from equations (20) and (21) with the inclusion of spatial harmonics.

Inductance calculations using equations (17) and (18) were achieved using trapezoidal numerical integration in MATLAB. In the evaluation of equations (17) and (18), the stator slots are held constant and the rotor is moved from 0 to 2π radians. To calculate stator to rotor winding inductances, the rotor winding function is shifted alongside the rotor for each computation point.

The stator phase A self-inductance and the phase A and phase B mutual inductance can also be expressed as seen in equations (26) and (27)

$$L_{asas} = L_{ls} + L_1 - L_2 \cos 2\theta_r \tag{26}$$

$$L_{asbs} = -\frac{1}{2}L_1 - L_2 \cos 2\left(\theta_r - \frac{\pi}{3}\right) \tag{27}$$

As stated in Krause et al. (2013), the magnetizing d- and q-axis inductances were given in equations (28) and (29)

$$L_{mq} = \frac{3}{2}\left(L_1 - L_2\right) \tag{28}$$

$$L_{md} = \frac{3}{2}\left(L_1 + L_2\right) \tag{29}$$

The inductances evaluated along the direct and quadrature axis are presented in equations (30) and (31).

$$L_d = L_{ls} + L_{md} \tag{30}$$

$$L_q = L_{ls} + L_{mq} \tag{31}$$

3. Results and Discussion

The section focuses on the results of the procedural calculation of the inductances of both machine models. Since the modelling was done in parts, that is modelling stator windings, rotor windings and the air gap, using the sinusoidal and the actual models it is ideal to show the various results before inductance calculations.
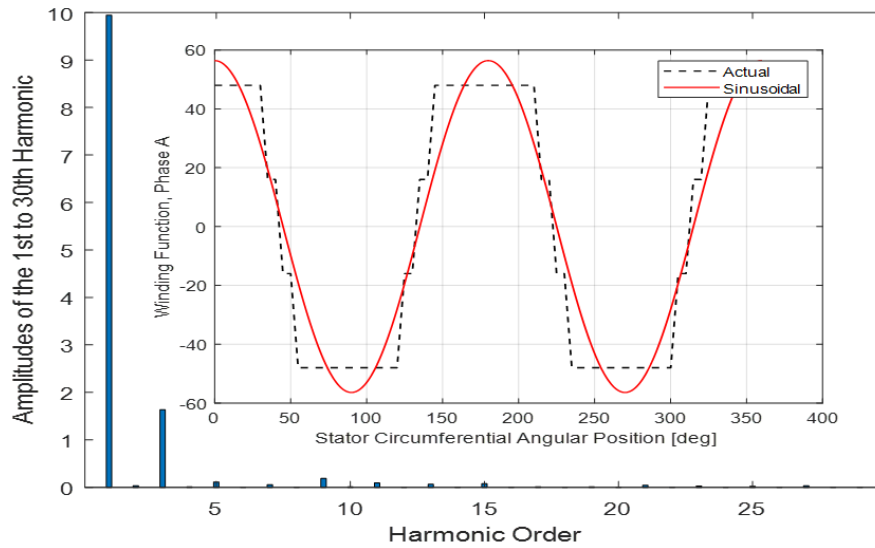
Figure 4: Phase A winding function of a 36-slot distributed stator winding showing the actual, sinusoidal and the harmonic spectrum

The phase A actual (including MMF harmonics) and sinusoidal winding function of the distributed winding configuration, and the harmonic spectra are shown in Figure 4. The winding function plot was achieved using equations (19) and (20).
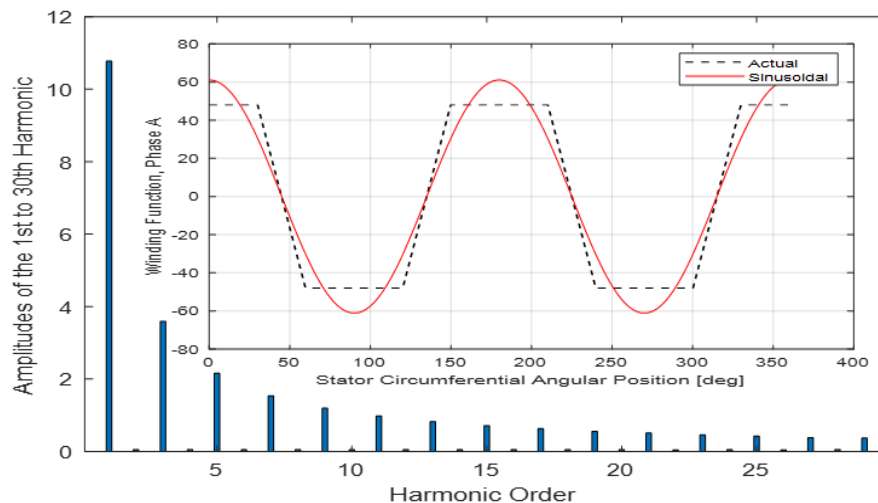
Figure 5: Phase A winding function of a 12-slot concentrated stator winding showing the actual, sinusoidal and the harmonic spectrum

The phase A actual (including MMF harmonics) and sinusoidal winding function of the concentrated winding configuration, and the harmonic spectra are shown in Figure 5. The winding function plot was also achieved using equations (19) and (20).

The concentrated winding configuration was seen to have more MMF harmonics than the distributed winding.
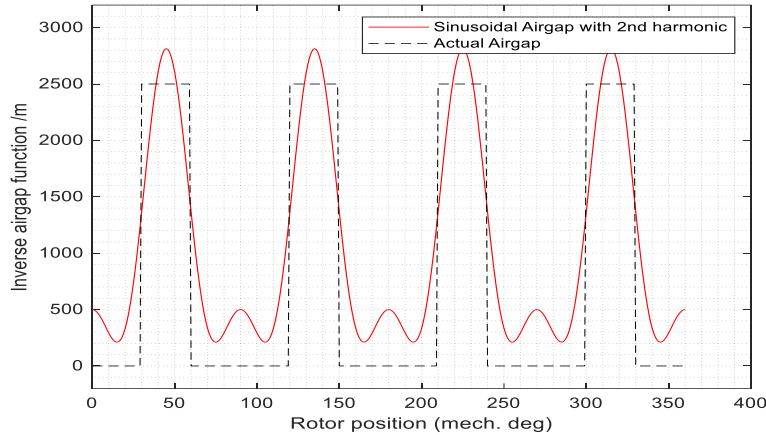
Figure 6: Inverse airgap function for actual and the sinusoidal considering only the second harmonic

The inverse airgap functions for the sinusoidal and the actual model of a synchronous reluctance machine having a 4-pole traditional dumbbell rotor, using the airgap dimensions as seen in Table 1 are presented in Figure 6. The sinusoidal plot was derived from equation (21), while the actual was done considering the airgap length at the pole face and the interpolar airgap.
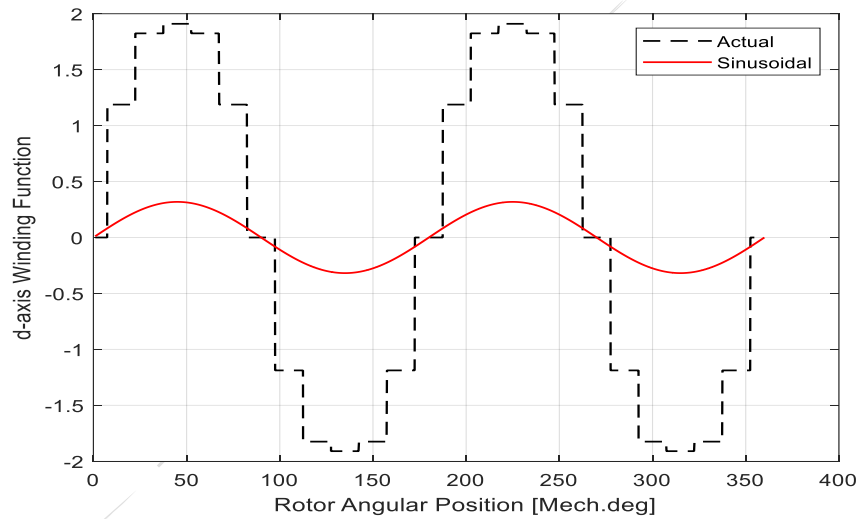
Figure 7: Fundamental components of d-axis cage winding expression, showing the actual and the sinusoidal

Using equations (22) and (24), the d-axis cage winding functions were derived as presented in Figure 7.
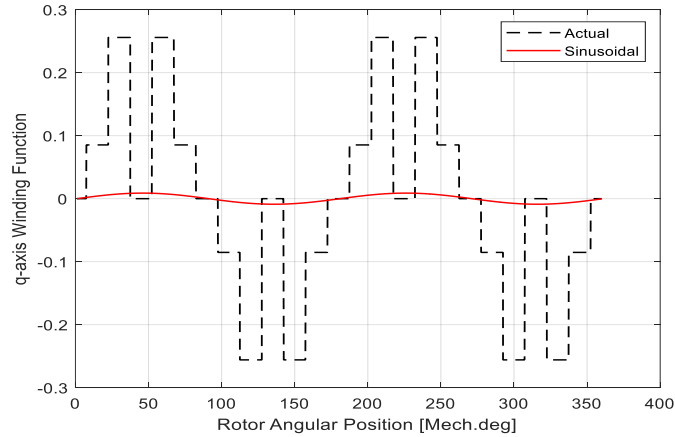
Figure 8: Fundamental components of q-axis cage winding expression, showing the actual and sinusoidal

While using equations (23) and (25), the q-axis cage winding functions were derived as presented in Figure 8.
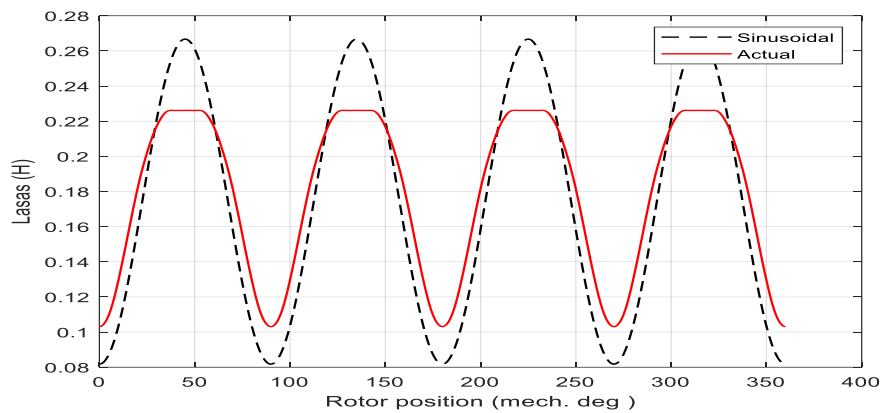
Figure 9: Self-inductance of distributed stator windings, for phase A

The actual and sinusoidal self-inductance of the distributed winding model is presented in Figure 9. The plots were achieved using trapezoidal numerical integration of equations (17) and (18) in MATLAB.
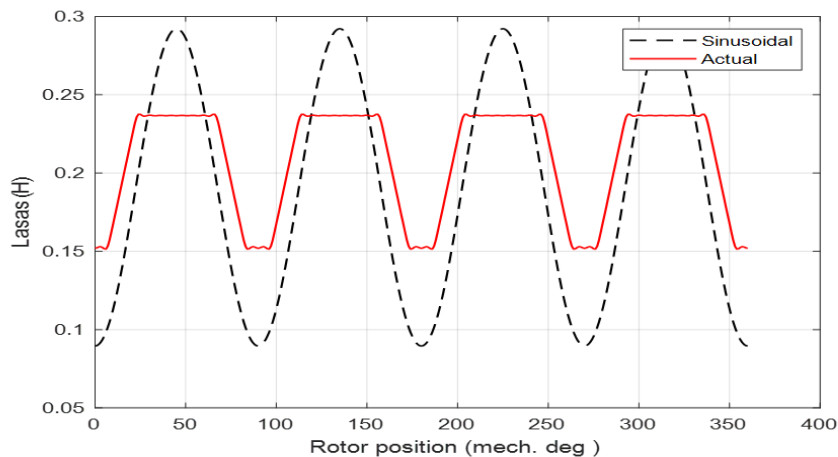
Figure 10: Self-inductance of concentrated stator windings, for phase A

The actual and sinusoidal self-inductance of the concentrated winding model is presented in Figure 10. The plots were also achieved using trapezoidal numerical integration of equations (17) and (18) in MATLAB.
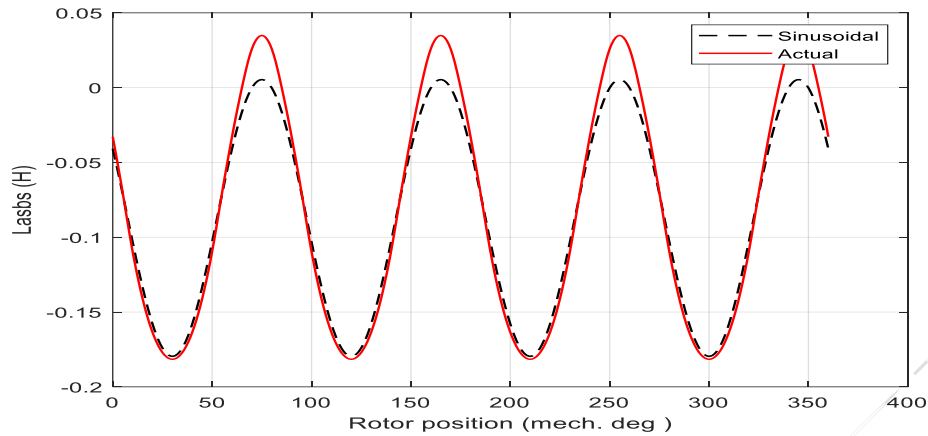
Figure 11: Mutual inductance between distributed stator winding, for phase A and phase B

The actual and sinusoidal mutual inductance for phase A and phase B of the distributed winding model is presented in Figure 11. The plots were calculated using trapezoidal numerical integration of equations (17) and (18) in MATLAB.
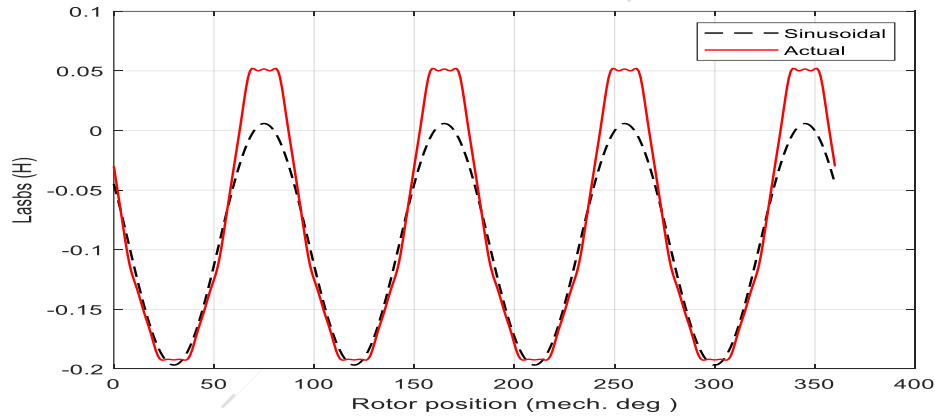
Figure 12: Mutual inductance between concentrated stator winding, for phase A and phase B

The actual and sinusoidal mutual inductance for phase A and phase B of the concentrated winding model is presented in Figure 12 derived from the trapezoidal numerical integration of equations (17) and (18) in MATLAB.
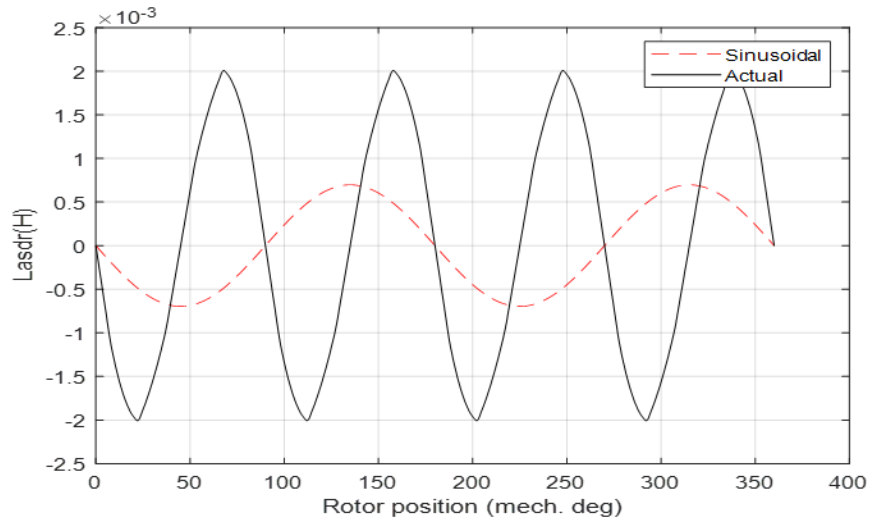
Figure 13: Mutual inductance between distributed stator winding, of phase A and d-axis winding

In Figure 13, the actual and sinusoidal stator to rotor mutual-inductances of the distributed stator winding phase A and the rotor d-axis winding were presented. The plots were calculated using trapezoidal numerical integration of equations (22) and (24) in MATLAB.
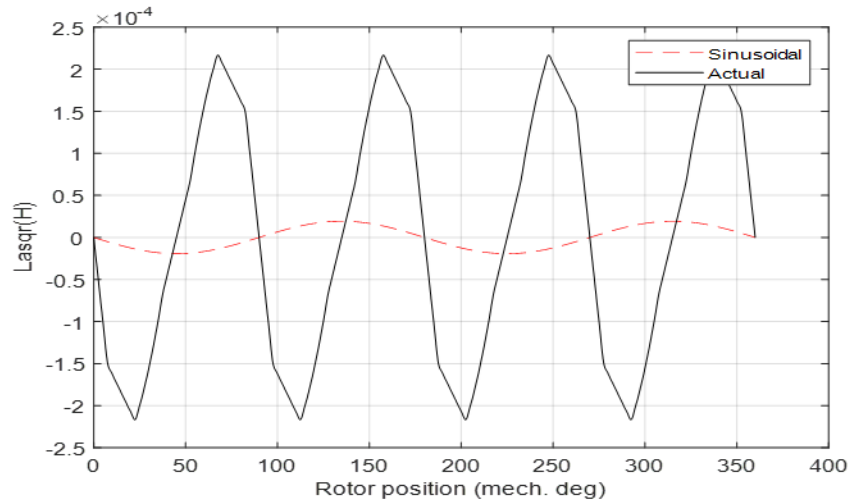
Figure 14: Mutual inductance between distributed stator winding, of phase A and q-axis winding

In Figure 14, the actual and sinusoidal stator to rotor mutual-inductances of the distributed stator winding phase A and the rotor d-axis winding were presented. The plots were calculated using trapezoidal numerical integration of equations (23) and (25) in MATLAB.
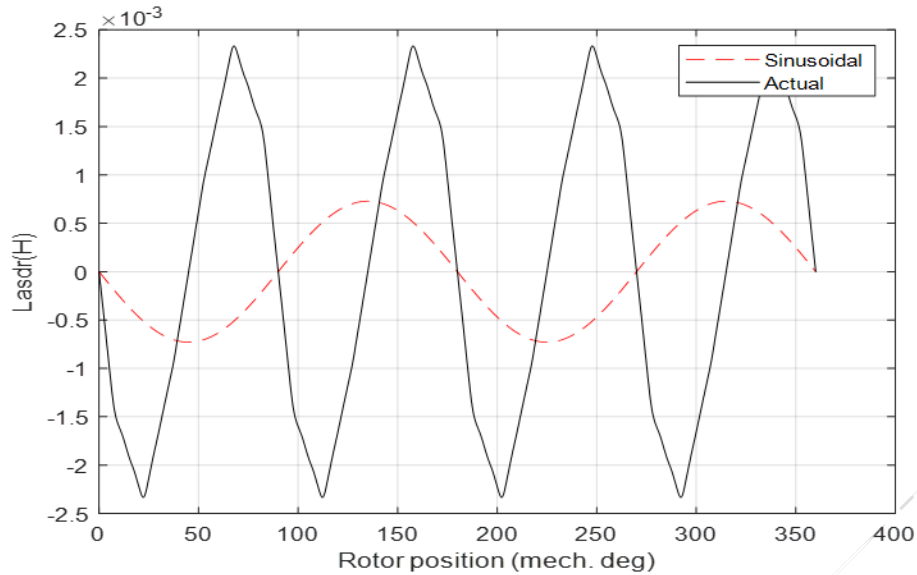
Figure 15: Mutual inductance between concentrated stator winding, of phase A and d-axis winding

Figure 15 shows the actual and sinusoidal stator to rotor mutual-inductances of the concentrated stator winding phase A and the rotor d-axis winding. The plots were calculated using also the trapezoidal numerical integration of equations (22) and (24) in MATLAB.
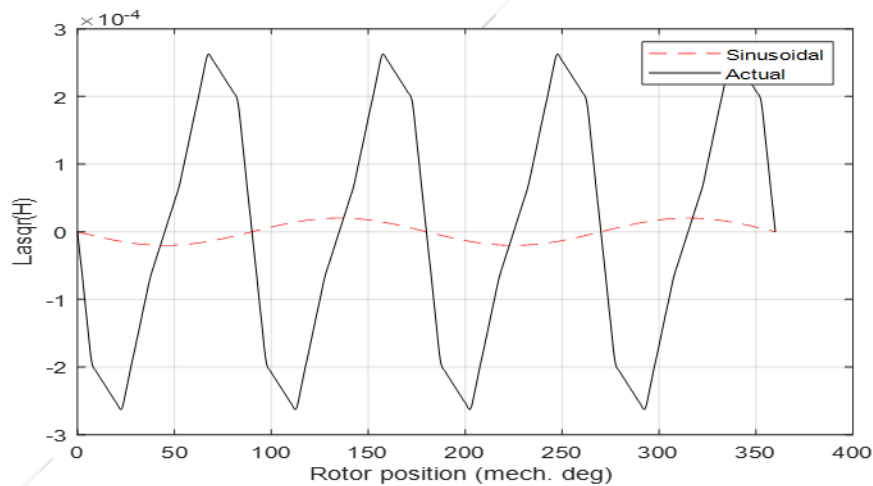
Figure 16: Mutual inductance between concentrated stator winding, of phase A and q-axis winding

In Figure 16, the actual and sinusoidal stator to rotor mutual-inductances of the concentrated stator winding phase A and the rotor d-axis winding were presented. The plots were calculated using trapezoidal numerical integration of equations (23) and (25) in MATLAB.

The magnetizing d-axis and q-axis inductances of the distributed and concentrated winding SynRM models were calculated from the self-inductance plots in Figures 9 and 10 and the results are shown in Table 2. The inductance coefficients L_1 and L_2 in equations (26) and (27) were derived

from the self-inductance plots and used to calculate the magnetizing d-axis and q-axis inductances using equations (28) and (29). The direct and quadrature axis inductance were later calculated using equations (30) and (31). The calculated results are presented in Table 2 for comparison.

Table 2. Calculated values of d- and q-axis inductances, saliency ratio and torque index

Winding	Calculated (Sinusoidal)				Calculated (Actual)			
	d-axis inductance (L_d)	q-axis inductance (L_q)	Saliency ratio (L_d/L_q)	Torque index (L_d-L_q)	d-axis inductance (L_d)	d-axis inductance (L_q)	Saliency ratio (L_d/L_q)	Torque index (L_d-L_q)
Distributed	404.48 mH	131.01 mH	3.09	273.47	350.18 mH	167.18 mH	2.10	183.0
Concentrated	449.18 mH	145.18 mH	3.09	304.0	366.28 mH	232.38 mH	1.58	133.9

From Table 2, the calculated sinusoidal saliency ratios are the same and the torque indexes were close compared to the actual saliency ratios and torque indexes. The actual saliency ratios were ideal as the distributed winding topology will have a better saliency ratio when compared to that of the concentrated winding. The reason for the better saliency is mainly because of the presence of harmonics in the concentrated windings.

4. Conclusion

This paper presented a numerical study comparing the inductances of concentrated and distributed winding synchronous reluctance motors (SynRMs) using two winding function theory-based methods. The actual winding function theory, which accounted for slot opening effects and spatial winding harmonics, was found to be more accurate than the sinusoidal method. The study revealed that the distributed winding topology outperformed the concentrated winding topology, showing a better saliency ratio and torque index. These findings have significant implications for SynRM design and optimization.

References

Al-Nuaim, NA. and Toliyat, HA. 1998. A novel method for modelling dynamic air -gap eccentricity in synchronous machines based on modified winding function theory. IEEE Transactions on Energy Conversion, 13(2): 156–162.

Faiz, J. and Tabatabaei, I. 2002. Extension of Winding Function Theory for Nonuniform Air Gap in Electric Machinery. IEEE Transactions on Magnetics, 38(6): 3654–3657.

Gojko, JM., Momir, DD. and Aleksandar, OB. 1999. Skew and linear rise of MMF across slot modelling - winding function approach. IEEE Transactions on Energy Conversion, 14(3): 315–320.

Houdouin, G., Barakat, G., Dakyo, B. and Destobbeleer, E. 2003. A winding function theory-based global method for the simulation of faulty induction machines. In Proceedings of the IEEE International Electric Machines and Drives Conference, Madison, WI, USA, 1–4 June 2003; no. 1, 297–303.

Jiang, H., Aggarwal, R., Weller, G., Ball, S. and Denning, L. 1999. A new approach to synchronous generator internal fault simulation using combined winding function theory and direct phase quantities. 9th International Conference on Electrical Machines and Drives, Canterbury, UK, 03-01 September 1999. no.468, 105–111.

Krause, PC., Wasynczuk, O., Sudhoff, SD. and Pekarek, SD. 2013. Analysis of electric machinery and drive systems. Wiley, Hoboken, New Jersey.

Liang, F., Xu, L. and Lipo, TA. 1991. Dq Analysis of a variable speed doubly AC Excited Reluctance Motor. Electric Machines & Power Systems, 19(2): 125-138.

Lipo, TA. 2012. Analysis of Synchronous Machines. Taylor & Francis Group, LLC, Boca Raton, Florida.

Lipo, TA. 2017. Introduction to AC Machine Design. Wiley, Hoboken, New Jersey.

Obe, ES. 2009. Direct computation of ac machine inductances based on winding function theory. Energy Conversion and Management, 50(3): 539–542.

Obe, ES. 2010. Calculation of inductances and torque of an axially laminated synchronous reluctance motor. IET electric power applications, 4(9): 783-792.

Obe, ES, and Binder, A. 2011. Direct-phase-variable model of a synchronous reluctance motor including all slot and winding harmonics. Energy Conversion and Management, 52: 284–291.

Obe, ES., Nnadi, DB., and Eke, J. 2009. Inductances and Airgap Flux Density of a Synchronous Reluctance Machine using the Actual Machine Geometry. NSE Technical Transactions, 44(1): 29–40.

Spargo, CM. 2016. Synchronous Reluctance Technology Part-II. MagNews, Durham Research Online, 44(2): 1–6.

Tabatabaei, I., Faiz, J., and Lesani, H. 2004. Modelling and Simulation of a Salient-Pole synchronous generator Using Modified Winding Function Theory. IEEE Transactions on Magnetics, 40(3): 1550–1555.

Toliyat, HA., Rahimian, MM., and Lipo, TA. 1991. Dq modelling of 5 phase reluctance machines including third harmonic IEEE Conference Record of the 1991 IEEE Industry Applications Society Annual Meeting - Dearborn, MI, USA, 28 September - 4 October 1991, 231-237.